Available online at www.sciencedirect.com
ScienceDirect
Trans. Nonferrous Met. Soc. China 35(2025) 105−125
Transactions of Nonferrous Metals Society of China
www.tnmsc.cn

Intricate interplay between shear stress and extrusion temperature in Mg−Al composite rods

Jian-xing ZHAO, Chao-wei ZENG, Ting YUAN, Wei PENG, Zhen-wei SUN, Ou ZHANG, Hong-jun HU

College of Materials Science and Engineering, Chongqing University of Technology, Chongqing 400054, China

Received 17 May 2023; accepted 19 September 2023

Abstract: The Mg−Al composite rods of aluminum core-reinforced magnesium alloy were prepared by the extrusion−shear (ES) process, and the microstructure, deformation mechanism, and mechanical properties of the Mg−Al composite rods were investigated at different extrusion temperatures and shear stresses. The experimental results show that the proportion of dynamic recrystallization (DRX) and texture for Al and Mg alloys are controlled by the combination of temperature and shear stress. The texture type of the Al alloys exhibits slight variations at different temperatures. With the increase of temperature, the DRX behavior of Mg alloy shifts from discontinuous DRX (DDRX), continuous DRX (CDRX), and twin-induced DRX (TDRX) dominant to CDRX, the dislocation density in Mg alloy grains decreases significantly, and the average value of Schmid factor (SF) of the basal ⟨*a*⟩ slip system increases. In particular, partial grains exhibit a distinct dominant slip system at 390 °C. The hardness and thickness of the bonding layer, as well as the yield strength and elongation of the Mg alloy, reach their maximum at 360 °C as a result of the intricate influence of the combined temperature and shear stress.

Key words: Mg−Al composite rod; texture evolution; deformation mechanism; intermetallic compound; extrusion−shear process

1 Introduction

Magnesium-based alloys, renowned for their lightweight nature, castability, and excellent mechanical properties, have been widely touted as promising materials for the aerospace and automotive industries [1−3]. Yet, their practical implementation has been hindered by the unfortunate fact that they suffer from numerous mechanical drawbacks, such as low ductility and toughness, and a regrettable susceptibility to corrosion [4,5]. To address these lamentable limitations, the researchers have delved into using magnesium-based composites to enhance their mechanical properties [6]. Among these composites, the one that stands out is the impressive Mg−Al, which blends magnesium sleeves with the aluminum core and thereby bolsters the strength and ductility of the Mg−Al composite materials by catalyzing the formation of fine and homogeneous microstructures [7−12]. Including In the aluminum core has the additional benefit of generating intermetallic compounds (IMCs) with magnesium, such as $Al_{12}Mg_{17}$ and Al_3Mg_2, which can further elevate the strength and hardness of alloy [13,14].

Among various processing techniques, extrusion is a popular method to fabricate Mg−Al composites due to its high efficiency, low cost, and easy operation [15−17]. During the extrusion process, the material undergoes plastic deformation under high pressure and high temperature, leading to variations in the microstructure and mechanical properties of the material [18−20]. The results of

Corresponding author: Hong-jun HU, Tel: +86-18996100916, Fax: +86-23-62568893, E-mail: hhj@cqut.edu.cn
https://doi.org/10.1016/S1003-6326(24)66668-9

these studies indicate that the texture of magnesium alloys remains unchanged. However, due to the advantages of the extrusion process, not only the grains of magnesium alloys are refined, but also their mechanical properties are also substantially improved.

The shear stress, as a crucial factor in the extrusion process, plays an essential role in determining the microstructure and mechanical properties of the magnesium-based alloy [21−26]. The introduction of shear stress during the extrusion process has been observed to induce severe plastic deformation (SPD) in Mg, which can significantly enhance the proportion of DRX while simultaneously weaken the {0001} basal texture present in magnesium alloys. Ultimately, these effects can lead to a notable improvement in the mechanical properties of the resultant material [23,25]. In addition, the extrusion temperature is also a critical processing parameter. It has a considerable influence not only on the shear stress but also on the rate of plastic deformation and the evolution of the microstructure of the material [27−31]. Elevated temperatures can enhance the flow of the material and decrease the deformation resistance, thus enabling a more uniform microstructure and improved mechanical properties [28,29]. WU et al [32] observed that the extrusion temperature and the contribution of various slip systems significantly influence the plastic deformation in magnesium alloys. Specifically, they found that the activation of {0001} basal ⟨*a*⟩ slip, $\{10\bar{1}0\}$ prismatic ⟨*a*⟩ slip, and $\{11\bar{2}0\}$ prismatic ⟨*c*⟩ slip is significantly affected by temperature. The activation of $\{11\bar{2}2\}$ pyramidal ⟨*c*+*a*⟩ slip is beneficial to coordinating further plastic deformation [28]. Nevertheless, excessively high temperatures can also result in the loss of strength and ductility of the material, and introduce defects such as cracks and voids [33,34].

Despite the growing research in Mg−Al composite rods, there is still limited knowledge about the role of shear stress in the extrusion process at different temperatures. Understanding the underlying mechanisms that govern the extrusion process can provide insights into the micro-structural evolution and mechanical properties of the resulting materials. This knowledge can be used to optimize the processing conditions for producing high-performance Mg−Al composite rods.

In light of these aforementioned concerns, the present study seeks to delve deeper into the intricate interplay between shear stress and extrusion temperature of Mg−Al composite rods. To this end, some analytical techniques, including scanning electron microscopy (SEM), X-ray diffraction (XRD), electron backscattered diffraction (EBSD), and mechanical testing, are harnessed to analyze the microstructural evolution and mechanical properties of the extruded samples. The anticipated findings of this research can provide a profound understanding of the complex deformation mechanisms that govern the extrusion process of Mg−Al composite rods, which, in turn, could unlock the potential for developing advanced processing strategies that could produce high-performance Mg−Al composite materials.

2 Experimental

2.1 Materials and processing methods

Figure 1 illustrates the schematic diagram of the extrusion−shear (ES) process. The hardness, thermal conductivity, melting point, and other factors of the magnesium and aluminum alloys directly affect the forming quality and utilization performance of the Mg−Al composite rods. Therefore, the comprehensive properties of both magnesium and aluminum alloys should be considered during the preparation of the Mg−Al composite rods [11]. In this study AZ31 magnesium alloy and AA6063 aluminum alloy were selected, and the elemental compositions of the AZ31 magnesium alloy and AA6063 aluminum alloy are presented in Table 1. Additionally, the presence of oxides and impurities on the surface of Mg and Al significantly influences the metallurgical bonding of the resulting Mg−Al composite rods. Therefore, prior to the combination of the AZ31 magnesium alloy sleeve and AA6063 aluminum alloy core, the surfaces of both materials should be subjected to oxide and impurity removal. The Mg−Al composite billet was positioned within the die, and a heating coil was wrapped around the outer surface of the die for real-time temperature monitoring using a thermocouple, thereby regulating the extrusion temperature. Subsequently, the ES process was conducted at a steady extrusion velocity of 5 mm/s for the preparation of the Mg−Al composite rod.

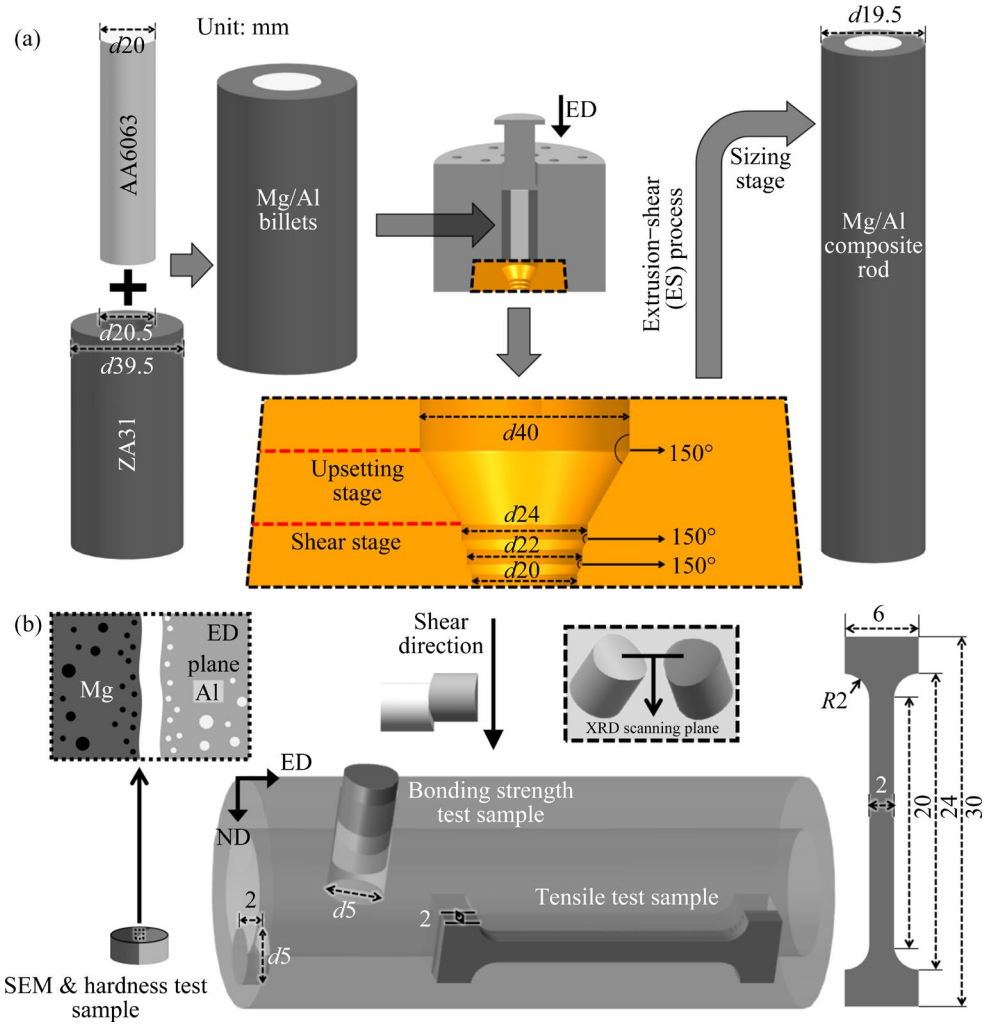

Fig. 1 Schematic diagram of preparation of Mg−Al composite rod by ES process (temperature: 330, 360, 390 °C) (a), and sampling location of various samples (b)

Table 1 Elemental compositions of AZ31 magnesium alloy and AA6063 aluminum alloy (wt.%)

Material	Mg	Al	Zn	Mn	Si	Fe	Cu
AZ31	Bal.	3.2	0.63	0.8	0.05	0.05	0.01
AA6063	0.58	Bal.	0.016	<0.01	0.43	0.06	<0.01

2.2 Mechanical properties test

The hardness samples were obtained from the Mg−Al composite rods along the normal direction (ND) and transverse direction (TD) (i.e., the ED plane), as illustrated in Fig. 1(b). The hardness of the samples were measured using an HVS-1000 microhardness tester (with a load of 1 N and a holding time of 10 s). Points were taken at intervals of 10 μm along the ND, with total 11 points per set. Each sample was subjected to three sets of hardness tests, and the average value was calculated to obtain the final hardness value.

The present study employed wire-cutting technique to obtain samples for bonding strength tests from Mg−Al composite rods prepared at different temperatures, as illustrated in Fig. 1(b). The samples were firmly secured using a specialized fixture and subjected to bonding strength tests at a rate of 3 mm/min. The experimentally obtained load was utilized to calculate the corresponding shear stress according to the formula:

$$\tau=F/A \quad (1)$$

where τ represents the bonding strength of the Mg−Al composite rods, F denotes the load, and A signifies the area of bonding layer.

Similarly, tensile test samples of magnesium alloy in Mg−Al composite rods at different temperatures were prepared using wire-cutting technique.

2.3 Microstructural characterization

The X-ray diffraction (XRD, PANalytical Empyrean Series 2) was utilized to perform phase analysis on the aluminum and magnesium sides of the sample separately. The scanning area of XRD was illustrated in Fig. 1(b). And JADE software was then employed to qualitatively analyze the phases of the bonding layer. SEM samples were obtained from the ED plane of Mg−Al composite rods. Before analysis, the surfaces were polished meticulously using water sandpaper (1400#) until they were devoid of any discernible scratches or blemishes. The JCM-7000 desktop tungsten filament scanning electron microscope (SEM) equipped with an energy dispersive spectrometer (EDS) was used to perform point scanning, line scanning, and surface scanning on the bonding layer of the SEM sample. To further investigate the evolution of the texture of the Mg−Al alloy and its bonding layer, the SEM sample was subjected to argon ion beam polishing using the argon ion polishing instrument (Fischione 1061). The SEM sample was then characterized using a field emission scanning electron microscope (ZEISS ΣIGMA HDTM) equipped with an EBSD detector, and the data was analyzed and processed using Channel 5 software.

3 Results and discussion

3.1 Microstructures of Mg and Al at different stages

The samples at 360 °C was selected and the microstructure variations of Mg−Al composite rods and its bonding layer throughout the ES process were observed. The inverse pole figure (IPF) maps, pole figure (PF), and IPF of Mg−Al alloys during the upsetting stage are depicted in Figs. 2(a, d). It can be observed that most of the aluminum grains exhibit a tendency towards the ⟨111⟩ direction, with a few tilting towards the ⟨001⟩ direction. As the upsetting region is subjected to a certain degree of shear stress along the ND, the aluminum alloy possesses a high density of dislocations, resulting in a predominance of dynamic recovery as the primary mechanism for softening, accompanied by the appearance of elongated grains. The maximum strength of the aluminum alloy texture is measured as 22.05. Conversely, most of the magnesium grains are inclined towards ⟨01 $\bar{1}$0⟩ and ⟨$\bar{1}$2 $\bar{1}$0⟩ directions, with a maximum texture strength of 25.46. In addition, due to the shear stress along the ND direction, the {0001} basal plane of most magnesium grains is parallel to the ND.

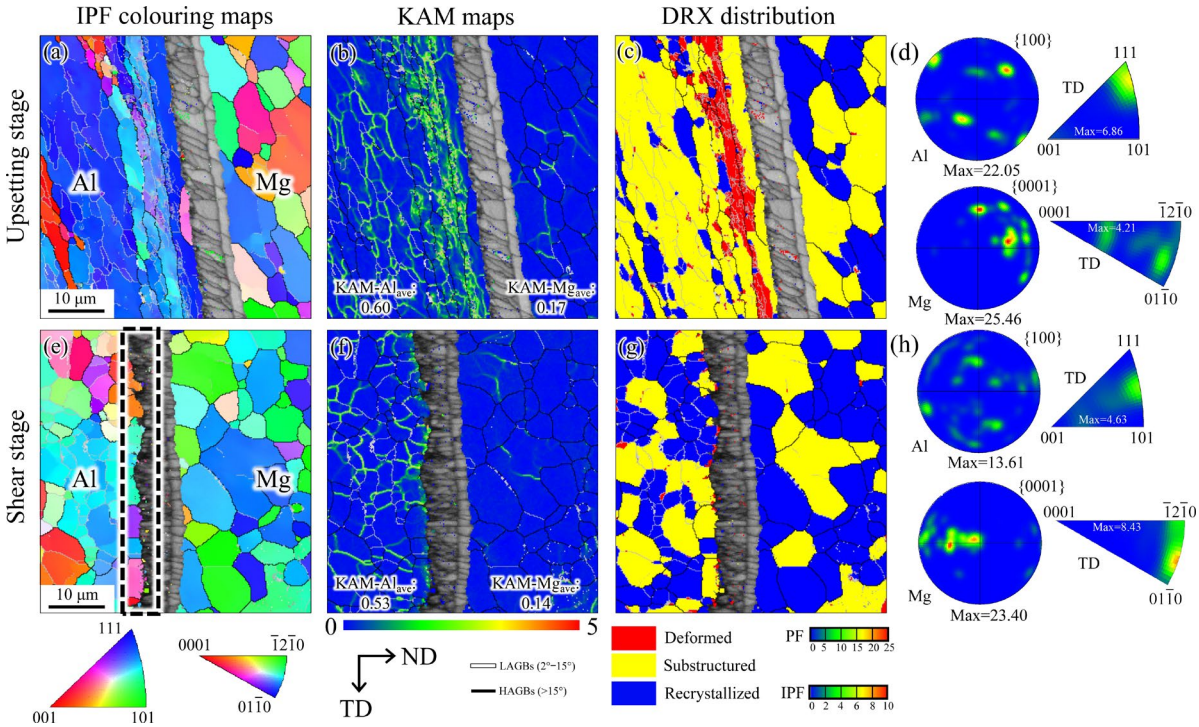

Fig. 2 Microstructures of Mg−Al composite rods at different stages: (a, e) IPF colouring maps; (b, f) KAM maps; (c, g) DRX distribution maps; (d, h) PF and IPF maps

As the extrusion process continues, when the Mg−Al alloys reach the shear stage, the PF and IPF of the Mg−Al alloys are shown in Figs. 2(e, h). The large shear stress in the shear stage causes the magnesium alloy grains to deflect along the ND and tilt towards $\langle \bar{1}2\bar{1}0 \rangle$ and $\langle 01\bar{1}0 \rangle$ directions. Meanwhile, the texture of the aluminum alloy becomes random, with most grains tilting towards the ⟨111⟩ and ⟨101⟩ directions. The increased diversity of texture types weakens the texture strength of the Mg and Al alloys. The texture strength of the aluminum alloy decreased to 13.61, while that of the magnesium alloy decreased to 23.40 and dispersed along the ND direction. The dislocations caused by the larger shear stress promoted the transformation of low-angle grain boundaries (LAGBs) to high-angle grain boundaries (HAGBs), and the softening mechanism of the aluminum alloy changed from dynamic recovery to DRX, while the proportion of DRX in the magnesium alloy further increased, as shown in Figs. 2(c, g). As DRX consumes dislocations, the kernel average misorientation (KAM) values of the Mg−Al alloys during the shear stage decreased compared to those during the upsetting stage, as shown in Figs. 2(b, f).

Furthermore, it should be noted that the simultaneous effects of high temperature and large shear stress not only cause the grain orientation of the aluminum alloy to become random but also result in an uneven interface morphology of the bonding layer on the Al side, as shown by the black dashed box in Fig. 2.

3.2 Microstructures of bonding layers at different temperatures

In the temperature range of 330−390 °C, as illustrated in Fig. 3, metallurgical bonding occurred in both AZ31 and AA6063 at sizing stage, as reported in other studies on the fabrication of the Mg−Al composites via diffusion bonding techniques [35−39]. The XRD scanning of the interface of Mg−Al composite rods was conducted on both the magnesium and aluminum sides. The JADE software was employed for phase analysis, which indicated the formation of an IMC of $Al_{12}Mg_{17}$ on the magnesium side and Al_3Mg_2 on the aluminum side, as illustrated in Fig. 4. Furthermore,

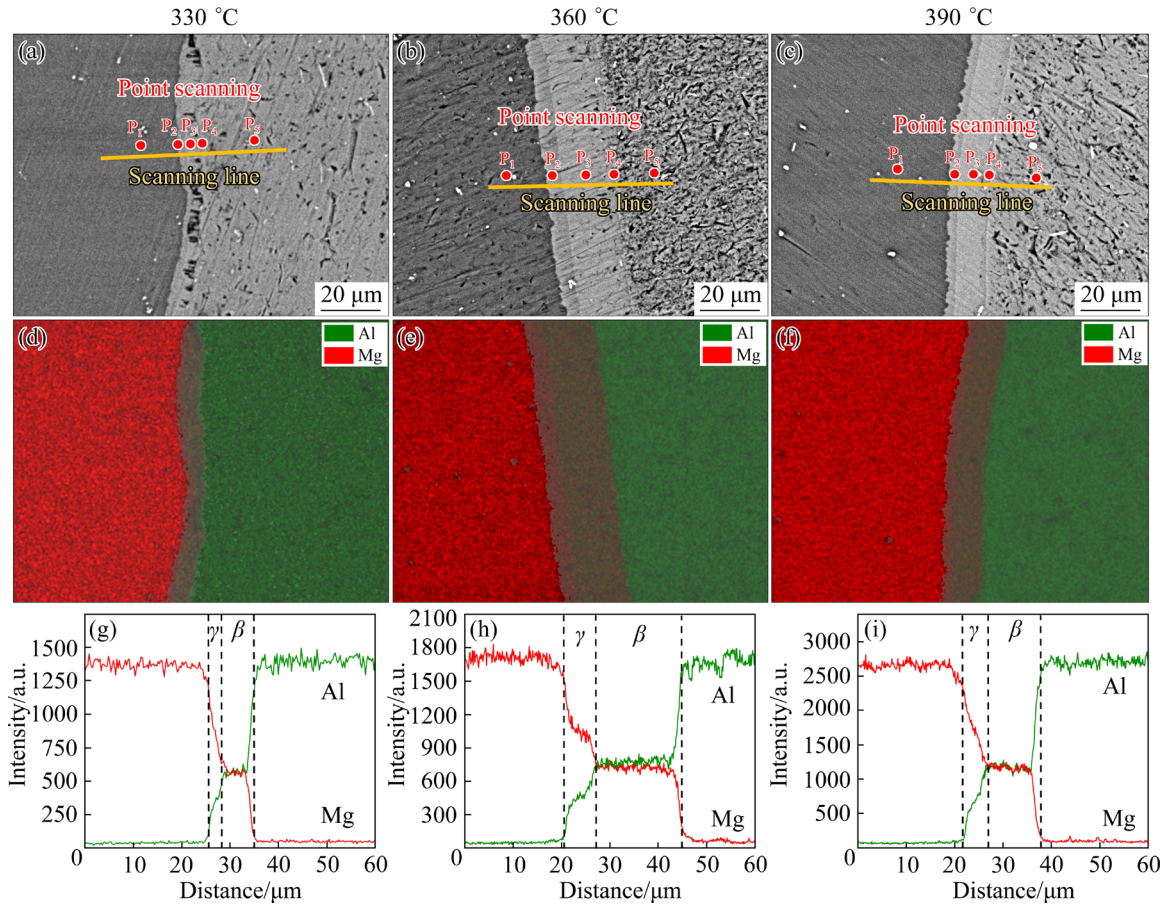

Fig. 3 Microstructures and EDS scanning results: (a−c) Microstructures; (d−f) Area scanning; (g−i) Line scanning

through a combination of Table 2 and the Mg−Al binary phase diagram, it was possible to further characterize the bonding layer of Mg−Al diffusion bonding as consisting of Mg (ss) − reaction layer (γ-$Al_{12}Mg_{17}$+β-Al_3Mg_2)−Al (ss) [40]. These results suggest that SPD could be produced through the extrusion process [23,25], and with the support of SPD and high temperature, diffusion of Mg and Al atoms occurred, leading to the formation of a metallurgical bond between Mg and Al. The gradient in atomic concentration resulted in different IMCs between Mg and Al. The growth of IMCs between Mg and Al can be described by the following equation [41−45].

The relationship between diffusion flux and concentration gradient can be expressed by Fick's first law equation, which establishes a connection between the two parameters:

$$J = -D\left(\frac{\mathrm{d}c}{\mathrm{d}x}\right) \tag{2}$$

where J represents the flux of atoms, D is the diffusion coefficient, and dc/dx is the concentration gradient. Furthermore, the diffusion coefficient equation allows the relationship among the diffusion coefficient, activation energy, and temperature to be determined [41,44]:

$$D = D_0 \exp\left(-\frac{Q}{RT}\right) \tag{3}$$

where D_0 is the pre-exponential factor, Q is the activation energy of diffusion, R is the molar gas constant, and T is the thermodynamic temperature. The relationship among these variables helps to

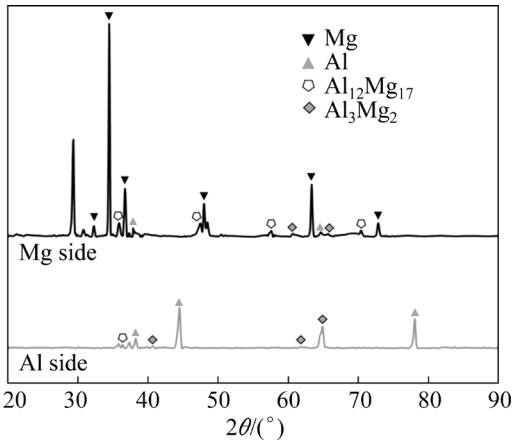

Fig. 4 XRD patterns of bonding layers in Mg−Al composite rods

Table 2 Element contents of points in Fig. 3

Temperature/°C	Point	Content/wt.%			Content/at.%		
		Mg	Al	O	Mg	Al	O
330	P_1	92.69±0.27	6.19±0.13	1.12±0.05	92.72±0.27	5.58±0.12	1.70±0.08
	P_2	53.72±0.21	44.67±0.28	1.61±0.06	55.72±0.22	41.72±0.26	2.53±0.10
	P_3	34.65±0.17	63.99±0.30	1.36±0.06	36.71±0.18	61.09±0.29	2.20±0.09
	P_4	10.58±0.09	86.10±0.28	1.74±0.06	11.48±0.09	84.17±0.27	2.88±0.11
	P_5	0.99±0.03	95.29±0.28	2.78±0.08	1.07±0.03	93.44±0.27	4.60±0.14
360	P_1	92.06±0.27	6.72±0.13	1.22±0.05	92.09±0.27	6.06±0.112	1.85±0.08
	P_2	46.00±0.19	52.88±0.29	1.12±0.05	48.24±0.20	49.97±0.28	1.79±0.09
	P_3	34.92±0.17	64.00±0.30	1.07±0.05	37.06±0.18	61.21±0.29	1.73±0.09
	P_4	32.09±0.16	61.10±0.28	3.85±0.10	33.59±0.17	57.61±0.27	6.12±0.15
	P_5	0.63±0.02	95.69±0.28	2.89±0.09	0.69±0.03	93.79±0.28	4.77±0.14
390	P_1	92.80±0.28	6.19±0.13	1.02±0.05	92.87±0.28	5.58±0.12	1.55±0.08
	P_2	51.95±0.21	46.71±0.29	1.34±0.06	54.07±0.21	43.81±0.27	2.12±0.09
	P_3	34.73±0.17	64.11±0.30	1.16±0.05	36.85±0.18	61.29±0.29	1.86±0.09
	P_4	9.35±0.09	83.50±0.28	5.38±0.11	9.92±0.09	79.79±0.27	8.66±0.18
	P_5	0.44±0.02	97.43±0.29	2.13±0.08	0.48±0.02	95.98±0.28	3.53±0.13

describe the behavior of atoms during the diffusion process, where the flux of atoms and the diffusion coefficient are directly proportional to the concentration gradient and the temperature, respectively.

Under the impact of temperature on the diffusion of Mg and Al, another parameter, shear stress must be considered. The severe plastic deformation due to shear stress can reduce the vacancy formation energy [46]. The equation for vacancy concentration (C_v) at thermal equilibrium is given as [46]

$$C_v = \exp\left(\frac{S_f}{k_B}\right)\exp\left(-\frac{E_f}{k_B T}\right) \quad (4)$$

where S_f is the entropy of vacancy formation, E_f is the energy of vacancy formation, and k_B is the Boltzmann constant. It is evident from the equation that if the vacancy formation energy is reduced by 20%, vacancy concentration and diffusion coefficient increase by four orders of magnitude.

The shear stress induces SPD, leading to atom movement, concentration gradient variations, and the formation of sub-grains and grain boundaries. These high-energy sites, including dislocations, grain boundaries, and interfaces, facilitate the diffusion of Mg and Al atoms. The manifestation of vacancies resulting from the diffusion of Mg and Al atoms further enhances their diffusion at these high-energy sites, contributing to the formation of IMCs between Mg and Al.

At 330 °C, gaps and minor defects in the bonding layer are attributed to the lower diffusion migration ability of Mg and Al atoms due to the relatively low temperature, as illustrated in Figs. 3(a, d, g). The Kirkendall effect causes more apparent defects on the Al side due to higher migration rate of Al atoms in the β-Al_3Mg_2 phase compared to Mg atoms [41]. Increasing the temperature enhances the diffusion ability of Mg and Al atoms, leading to a thicker bonding layer at 360 °C. The lower activation energy for the growth of β-Al_3Mg_2 (~86 kJ/mol) compared to γ-$Al_{12}Mg_{17}$ (~165 kJ/mol), along with its higher inter-diffusion coefficient and lower activation energy, results in a larger thickness of β-Al_3Mg_2, as illustrated in Figs. 3(b, e, h) [44]. At 390 °C, despite the further enhanced diffusion ability of Mg and Al atoms, the shear stress between Mg and Al weakens due to increased plasticity of Mg, resulting in a reduction of high-energy sites. This leads to a significant decrease in the diffusion of Mg and Al atoms compared to that at 360 °C, causing a thinner bonding layer. The Al content at Point P_2 (i.e., γ-$Al_{12}Mg_{17}$) at 360 °C is significantly higher than at the other temperatures, as given in Table 2. The importance of shear stress is further confirmed, considering the higher diffusion coefficient of Al atoms and significant shear strain caused by higher shear stress, as illustrated in Fig. 5.

The EBSD scanning of samples reveals variations in energy distribution, DRX, and texture evolution of IMCs at different temperatures. The dislocation pile-up on the Mg side of the bonding layer decreases, resulting in lower dislocation density and KAM value [47]. The Mg side appears blue, indicating low stored energy and dislocation density. The average KAM value is slightly higher at 360 °C. The temperature has a significant influence on DRX, with the proportion of DRX being proportional to temperature, as illustrated in Fig. 6, the proportion of deformed grains in the bonding layer decreases with increasing temperature. The grains in the bonding layer show no obvious preferred orientation and exhibit complete randomness.

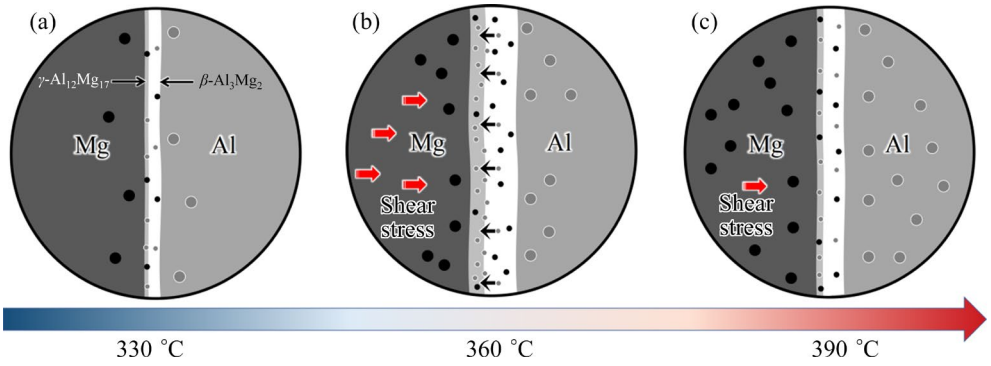

Fig. 5 Diffusion mechanism at different temperatures: (a) 330 °C; (a) 360 °C; (a) 390 °C

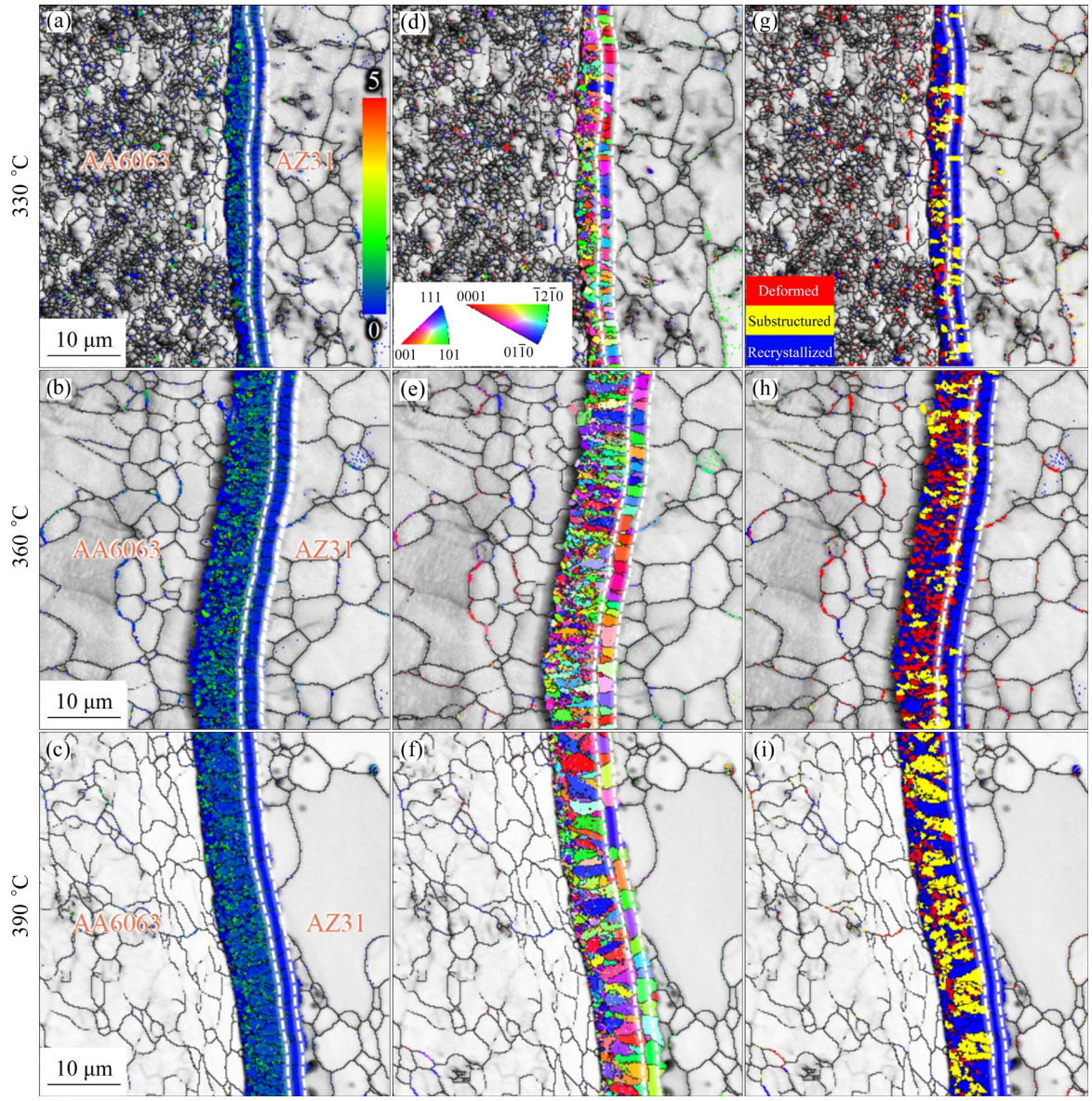

Fig. 6 EBSD results of bonding layer: (a−c) KAM maps; (d−f) IPF colouring maps; (g−i) DRX distribution maps

3.3 Texture evolution of Al alloy and Mg alloy at different temperatures

As depicted in Fig. 7(a), at 330 °C, the majority of aluminum alloy grains tend to align with the ⟨111⟩ direction, with a small fraction aligning with the ⟨001⟩ direction. This can be attributed to the prevalence of deformed grains in aluminum alloys at this temperature, which leads to grain fragmentation and randomization of grain orientations. Consequently, the maximum strength of {100} texture of aluminum alloy, under these conditions, is 16.35, which is the lowest among the three different preparation temperatures in this study. Upon increasing the preparation temperature to 360 °C, a concentrated distribution of grain orientations in the ⟨111⟩ and ⟨001⟩ directions is observed, resulting in a texture strength of 22.6 for the {100} plane of aluminum alloy, as illustrated in Fig. 7(b). Subsequently, at a temperature of 390 °C, nearly all of the aluminum alloy grains tend to align with the ⟨111⟩ direction, which can be attributed to the substantial increase in the plasticity of magnesium alloy at this temperature and the corresponding reduction in shear stress acting on the aluminum. Consequently, the aluminum alloy experiences relatively uniform extrusion forces, leading to nearly all of its grains aligning with the ⟨111⟩ direction. The {100} texture strength of aluminum alloy at this temperature increases to 35.25, as illustrated in Fig. 7(c). To

further analyze the variation of the texture type of the aluminum alloy, the texture of the aluminum alloy was determined by the ODF (orientation distribution function) maps, as shown in Fig. 8. It is remarkable that at 360 °C, due to the simultaneous effect of higher temperature and shear stress, there

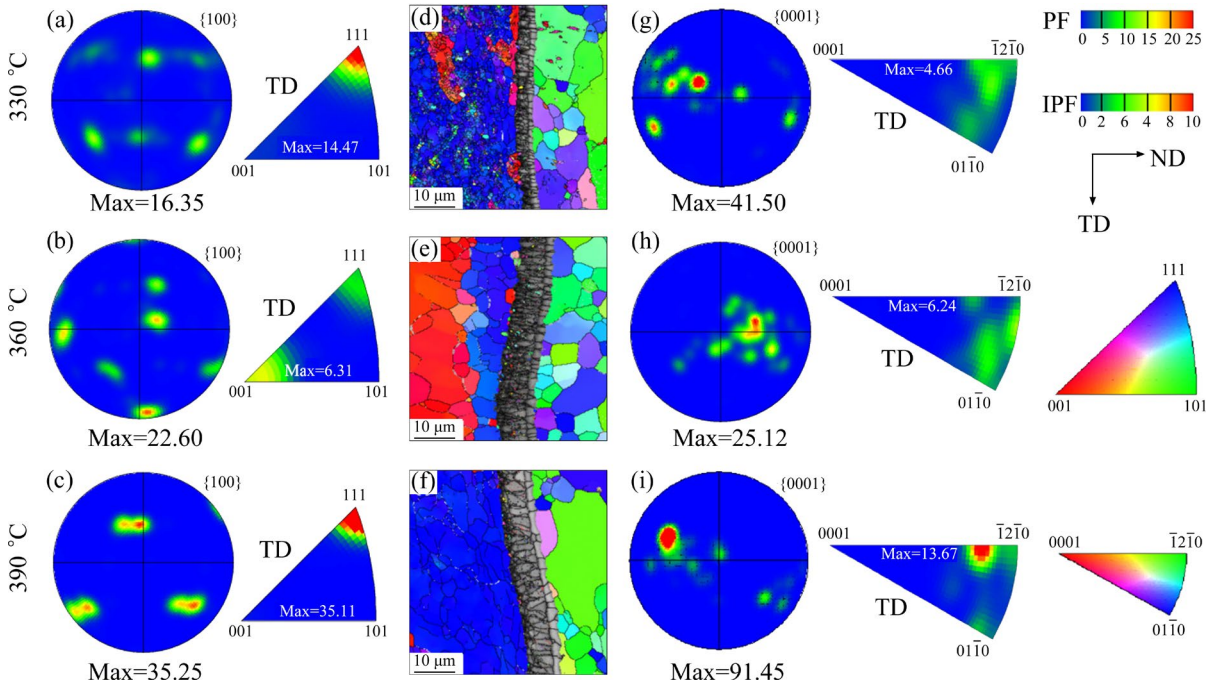

Fig. 7 Pole figure (PF) and inverse pole figure (IPF) maps of Al (a−c); IPF colouring maps of Al and Mg (d−f); PF and IPF maps of Mg (g−i)

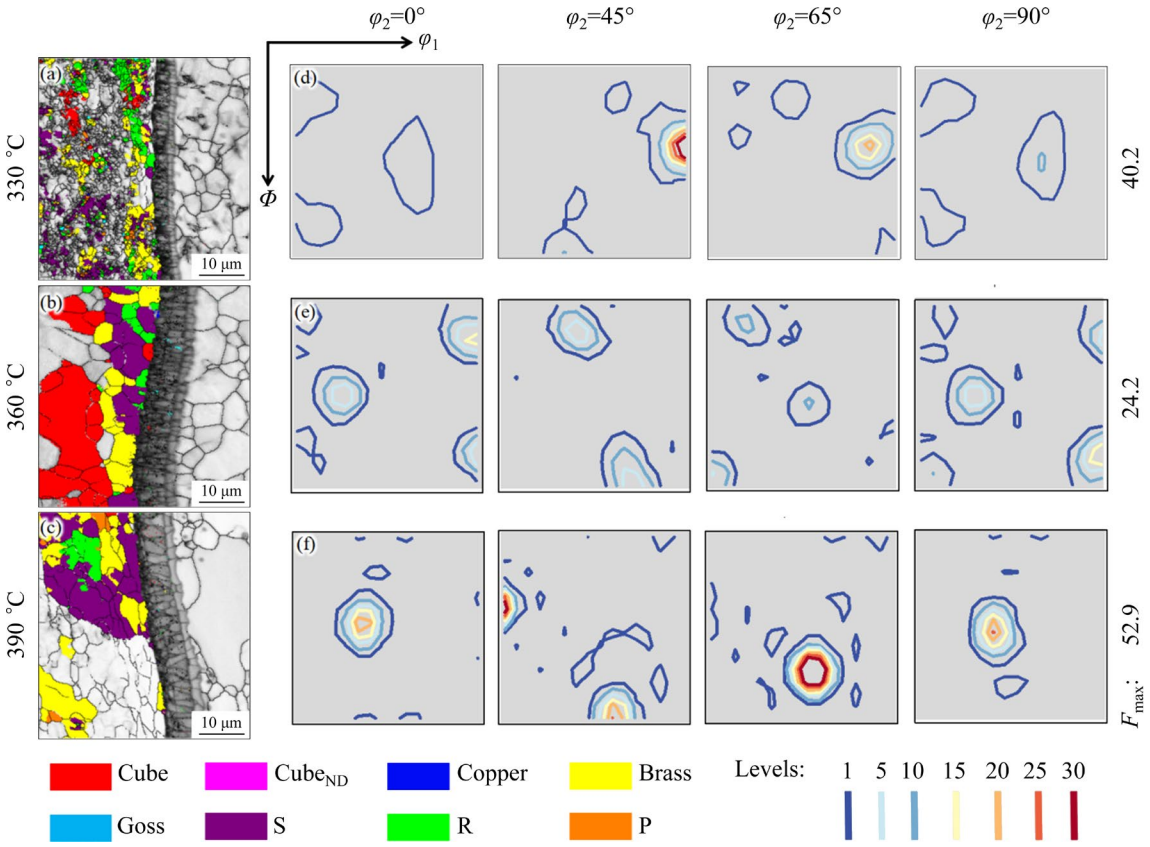

Fig. 8 Evolution of Al textures at different temperatures: (a−c) IPF colouring maps; (d−f) ODF maps

is a significant recrystallization texture of the aluminum alloy (Cube {001}⟨100⟩ texture). Furthermore, despite the significant impact of temperature on the texture type of the aluminum alloy, the Brass {011}⟨211⟩, S {123}⟨634⟩, and R {124}⟨211⟩ textures appear on the aluminum alloy at all three different temperatures and are relatively evenly distributed, as given in Table 3.

Furthermore, as evident from Figs. 7(g–i), as the preheating temperature is increased from 330 to 390 °C, the {0001} basal texture strength of magnesium alloy decreases from 41.5 to 25.12 before finally increasing to 91.45. This can be attributed to the DRX of magnesium alloy becoming sufficiently dominant at 360 °C, leading to the deviation of the orientation of the DRXed grains under the influence of high temperature and stress, resulting in randomization of orientations of a few grains and a decrease in the strength of {0001} basal texture of magnesium alloy. However, as the temperature is further increased to 390 °C, grains begin to grow under high temperature conditions, as illustrated in Fig. 7(f). A few grains possessing preferred orientations (or randomly oriented grains) dominate in the {0001} basal texture of magnesium alloy within a certain range, leading to a sharp increase in the texture strength of magnesium alloy. Preferred orientations of magnesium alloy grains are observed in the $\langle 01\bar{1}0\rangle$ and $\langle \bar{1}2\bar{1}0\rangle$ directions, with a small proportion of grains tilting towards $\langle 02\bar{2}1\rangle$ and $\langle \bar{1}2\bar{1}1\rangle$ directions.

Table 3 Euler angles and proportions of different types of Al textures

Temperature/°C	Texture type	{*hkl*}⟨*uvw*⟩	Euler angle/(°)			Fraction/%
			φ_1	Φ	φ_2	
330	Cube	{001}⟨100⟩	0	0	0	1.48
	$Cube_{ND}$	{001}⟨110⟩	45	0	0	0.16
	Copper	{112}⟨111⟩	90	35	45	0.28
	Brass	{011}⟨211⟩	35	45	90	12.20
	Goss	{011}⟨100⟩	0	45	90	0.20
	S	{123}⟨634⟩	59	37	63	9.63
	R	{124}⟨211⟩	57	29	63	4.61
	P	{110}⟨221⟩	59	45	0	0.61
360	Cube	{001}⟨100⟩	0	0	0	19.40
	$Cube_{ND}$	{001}⟨110⟩	45	0	0	−
	Copper	{112}⟨111⟩	90	35	45	0.09
	Brass	{011}⟨211⟩	35	45	90	16.40
	Goss	{011}⟨100⟩	0	45	90	0.06
	S	{123}⟨634⟩	59	37	63	10.20
	R	{124}⟨211⟩	57	29	63	2.09
	P	{110}⟨221⟩	59	45	0	0.03
390	Cube	{001}⟨100⟩	0	0	0	0.14
	$Cube_{ND}$	{001}⟨110⟩	45	0	0	−
	Copper	{112}⟨111⟩	90	35	45	−
	Brass	{011}⟨211⟩	35	45	90	26.8
	Goss	{011}⟨100⟩	0	45	90	−
	S	{123}⟨634⟩	59	37	63	15.5
	R	{124}⟨211⟩	57	29	63	2.58
	P	{110}⟨221⟩	59	45	0	0.89

3.4 DRX variations of Al alloy and Mg alloy at different temperatures

At 330 °C, most aluminum alloy grains exhibit deformed structure, while the magnesium alloy grains are dominated by sub-structured grains. The plasticity of aluminum alloys and magnesium alloys at this temperature is inferior, dislocation slip is difficult, and a large amount of dislocation buildup occurs. The obvious twins appear, as illustrated in Fig. 9(c), which plays a coordinating role in the deformation of magnesium alloy. With the increase of temperature (i.e., up to 360 °C), DRX nucleation is facilitated. and DRX consumes a large amount of dislocations. This leads to an increase in the DRX proportion of magnesium and aluminum alloys while the KAM value decreases. It is remarkable that with a further increase in temperature, the shear stress for aluminum alloy decreases significantly. The DRX proportion of the aluminum alloy decreases paradoxically, and the KAM value increases to a certain extent. As the temperature reaches the critical value, i.e., 360 °C, the effect of shear stress on the DRX of the aluminum alloy is significantly stronger than the effect of temperature, as illustrated in Figs. 9 and 10(a, b, d, e).

In addition, recrystallization and grain growth

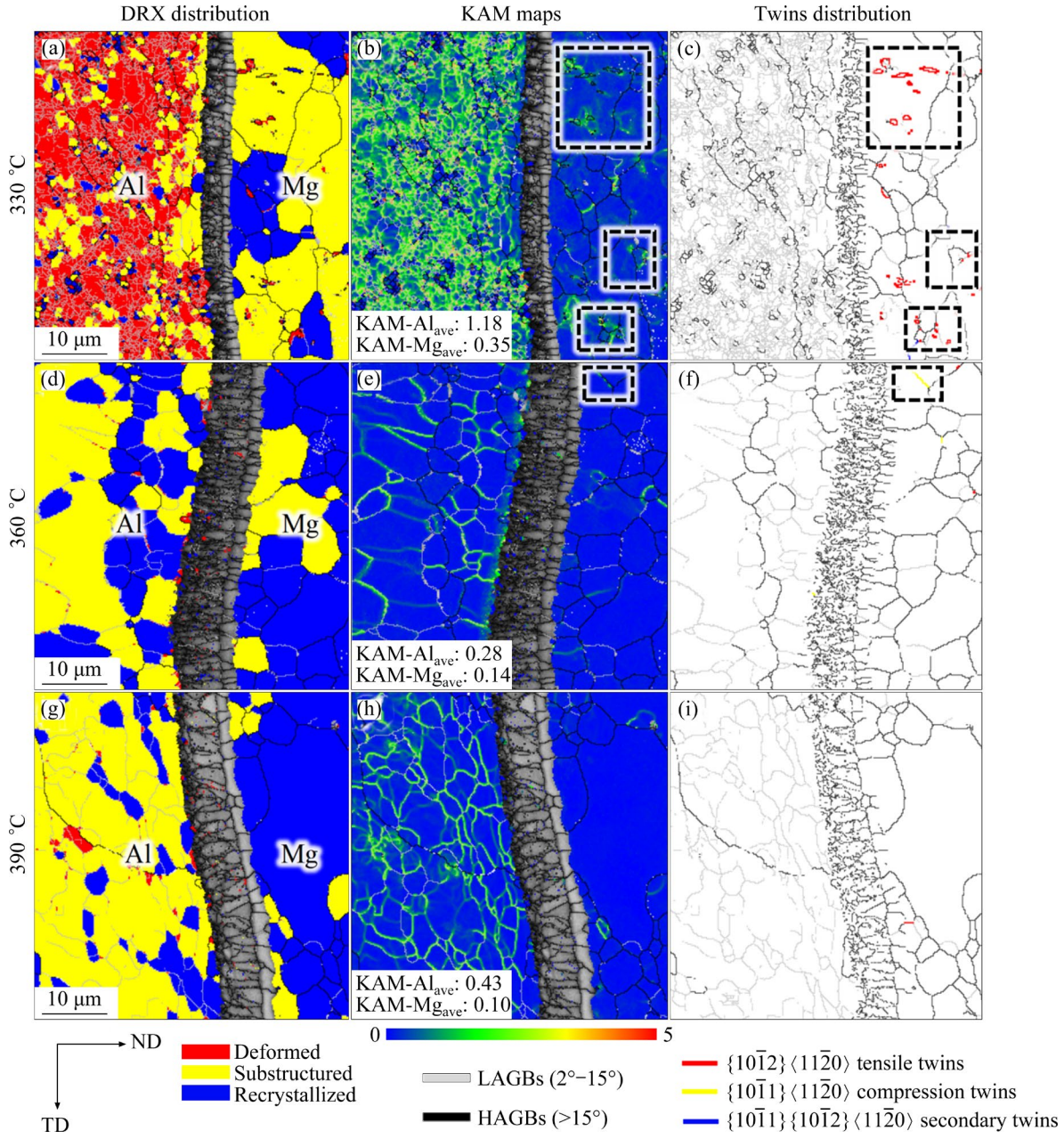

Fig. 9 Microstructures of Mg−Al composite rods ES-processed at different temperatures: (a, d, g) DRX distribution; (b, e, h) KAM maps; (c, f, i) Twins distribution

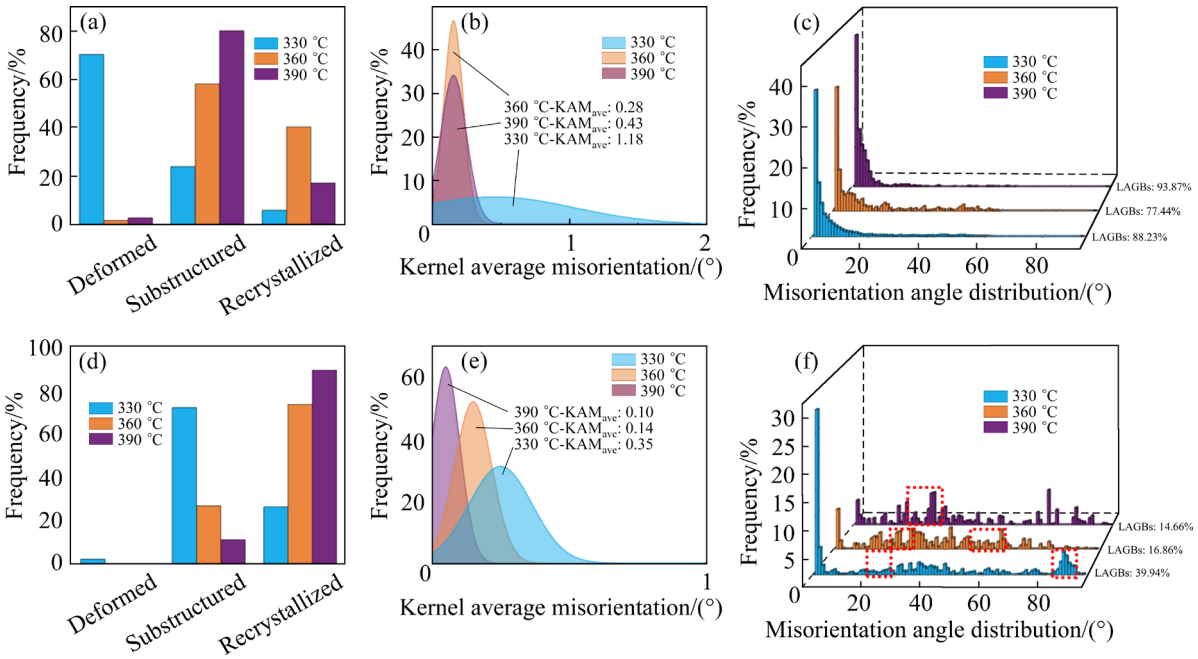

Fig. 10 DRX statistics (a, d); KAM statistical distribution maps (b, e) and statistical diagrams of misorientation angle distribution (c, f) of Al (a−c) and Mg (d−f) alloys

in hexagonal closed-packed (HCP) structured materials typically lead to a rotation of the orientation around the *c*-axis by 25°−35°. It can be seen that there are obvious peaks around 25° for different temperatures (i.e., DRX behavior). At 330 °C, there are prominent peaks around 83°−89°, and at 360 °C, a peak is observed near 56°, as illustrated in Fig. 10(f). These results provide evidence for the presence of significant $\{10\bar{1}2\}\langle 11\bar{2}0\rangle$ tensile twins and a small amount of $\{10\bar{1}1\}\langle 11\bar{2}0\rangle$ compression twins at 330 and 360 °C, respectively. However, it is interesting to note that the degree of accumulation of local dislocations near $\{10\bar{1}2\}\langle 11\bar{2}0\rangle$ tensile twins and $\{10\bar{1}1\}\langle 11\bar{2}0\rangle$ compression twins in magnesium alloys is significantly higher, as illustrated in Figs. 9(b, c, e, f).

3.5 Effect of temperature on DRX behavior of Mg alloy

In order to investigate the effects of shear stress and temperature on grain growth of Mg alloy, the DRX behavior at different temperatures was studied, and the misorientation was statistically analyzed. As shown by the white arrow in Fig. 11(a), the grain boundary exhibits a jagged and bow-shaped protrusion, indicating the presence of discontinuous DRX (DDRX). DDRX is known for its uneven microstructure transformation and long-range migration of large-angle grain boundaries, which can be observed as jagged and bulging large-angle grain boundaries. At 330 °C, due to the lower extrusion temperature, DDRX mechanism is favored, which significantly suppresses grain growth. Therefore, DDRX can be observed clearly at 330 °C. Furthermore, the misorientation in Figs. 11(g−i) increases along the ND, and the cumulative misorientation reaches 13.46°, which is much higher than the cumulative misorientation at the other two temperatures. However, as shown by the black arrow in Fig. 11(a), there are obviously DRXed grains wrapped by large grains. As mentioned earlier, as illustrated in Fig. 10, the proportion of LAGBs at 330 °C is high, which also confirms the existence of continuous DRX (CDRX). The accumulation of local dislocations near the twin boundaries leads to a noticeable increase in dislocation density, as illustrated in Fig. 9, which provides favorable conditions for DRX nucleation with high dislocation density. This confirms that twin-induced DRX (TDRX) is also a mechanism for DRX at this temperature. As the temperature increases, twins may be consumed by DRX and thus are seldom preserved. This indicates that the influence of twinning on DRX weakens with increasing temperature. It is worth noting that most of the original grain boundaries remain smooth and rarely become jagged, as illustrated in Figs. 11(b, c).

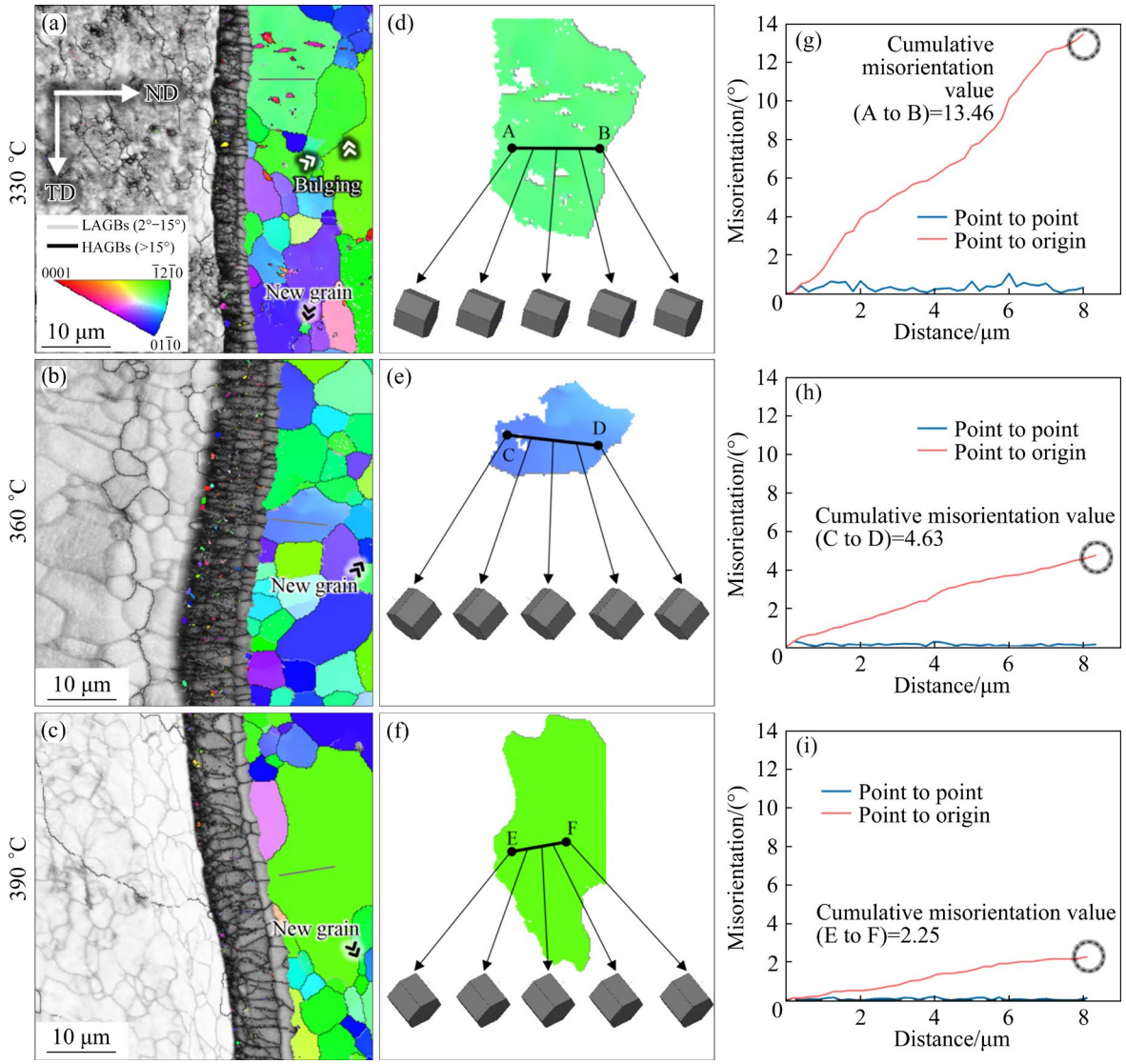

Fig. 11 IPF colouring maps (a−c), selected grains (d−f) and cumulative misorientation (g−i) of Mg alloy

The disappearance of the 83°−86° peak and the decrease in the proportion of LAGBs demonstrate the disappearance of twinning and the behavior of recrystallization absorbing dislocations. All these features prove that CDRX dominates the DRX mechanism at 360 and 390 °C. Therefore, at 330 °C, DDRX, CDRX, and TDRX jointly dominate the DRX mechanism, while at 360 and 390 °C, CDRX dominates the DRX mechanism.

3.6 Effect of temperature on deformation mechanism of Mg alloy

As previously discussed, the Schmid factor (SF) value of a slip system is inversely proportional to the critical resolved shear stress (CRSS) required to initiate the slip system [48,49]. Thus, a higher SF value indicates a lower CRSS and an easier initiation of the slip system. In the case of magnesium alloys, slip deformation is prone to occur when most grains are in a soft orientation state (SF value >0.2). Consequently, the SF average value can be utilized to roughly determine the type of slip system activated in magnesium alloys. The SF values of different slip systems at different temperatures are presented in Fig. 12. The SF average value of the basal ⟨*a*⟩ slip system is positively correlated with temperature, indicating that higher temperatures can further activate the basal ⟨*a*⟩ slip system, as illustrated in Figs. 12(a, e, i). In contrast, there is no general rule governing the influence of temperature on the SF values of non-basal ⟨*a*⟩ slip systems (i.e., the prismatic ⟨*a*⟩ slip system, pyramidal I ⟨*a*⟩ slip system, and pyramidal II ⟨*c*+*a*⟩ slip system).

The analysis of the IGMA measurement values obtained in experiments combined with the Taylor axis of the prescribed slip systems facilitates the determination of the primary deformation mechanism of the grain structure in magnesium alloys [50−52]. The Taylor axis of different slip systems of Mg alloys is given in Table 4. The distribution of IGMA in magnesium alloys typically falls into one of four categories: uniform IGMA distribution (any distribution with maximum IGMA intensity less than 2 mud), ⟨0001⟩-type IGMA distribution (peaks near the ⟨0001⟩ axis), ⟨*uvt*0⟩-type IGMA distribution (peaks near the ⟨*uvt*0⟩ axis), and others (distribution types that do not belong to the previous three). As illustrated in Figs. 13(g, h), most grains in magnesium alloys at 330 and 360 °C exhibit uniform IGMA distribution. These grains do not have a dominant slip system, and their deformation is regulated by the simultaneous activation of various slip systems. In addition, at 330 °C, there is significant occurrence of twinning. These twins play a certain coordinating role in the deformation of the grains. The deformation mechanism of the grain structure in magnesium

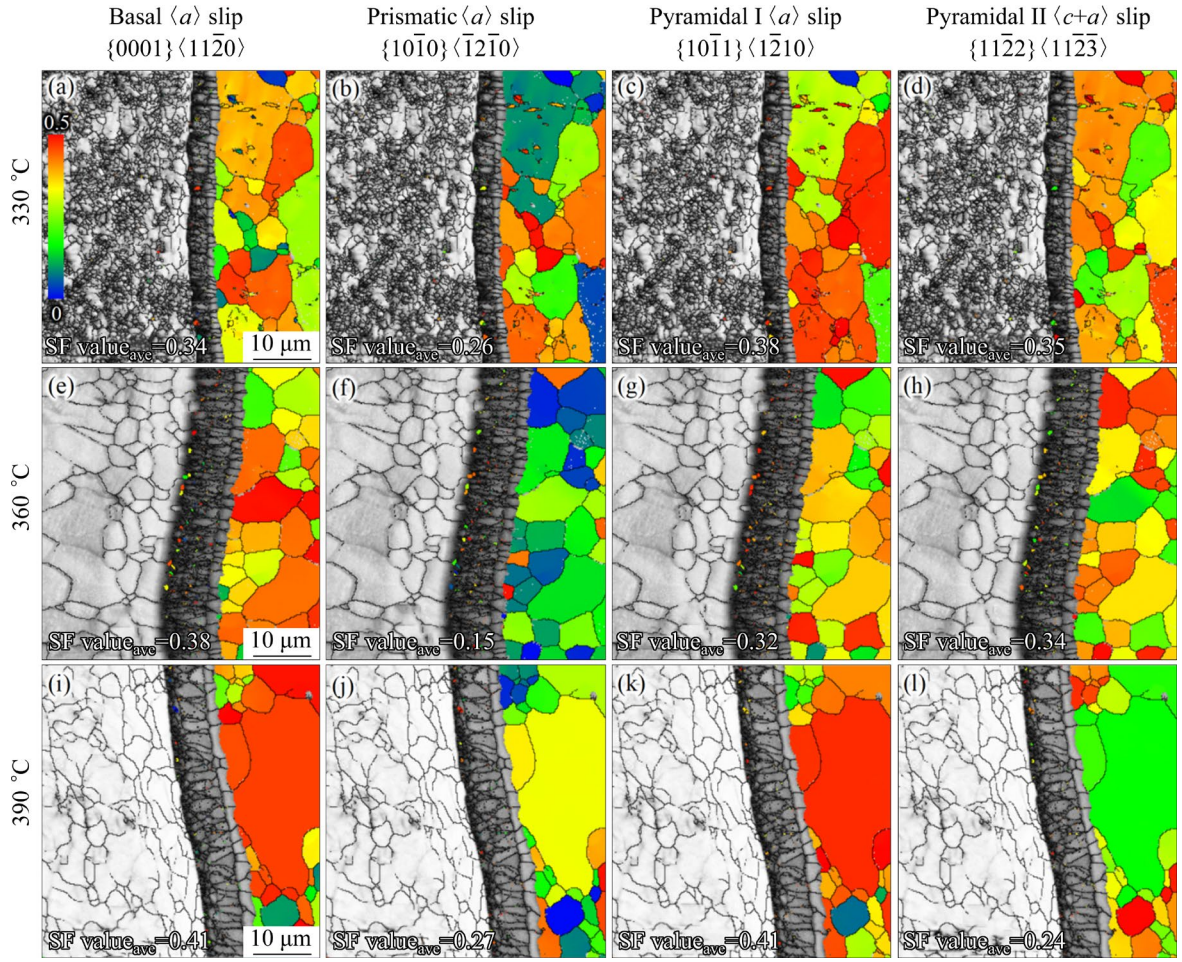

Fig. 12 SF value of basal ⟨*a*⟩ slip, prismatic ⟨*a*⟩ slip, pyramidal I ⟨*a*⟩ slip and pyramidal II ⟨*c*+*a*⟩ slip systems at different temperatures

Table 4 Taylor axis of different slip systems

Deformation mode	Total number of slip variants	Taylor axis	Total number of variants of Taylor axis
Basal ⟨a⟩ slip {0001}⟨11$\bar{2}$0⟩	3	⟨1$\bar{1}$00⟩	3
Prismatic ⟨*a*⟩ slip {10$\bar{1}$0}⟨$\bar{1}$2$\bar{1}$0⟩	3	⟨0001⟩	1
Pyramidal I ⟨*a*⟩ slip {10$\bar{1}$1}⟨1$\bar{2}$10⟩	6	⟨0$\bar{1}$12⟩	6
Pyramidal I ⟨*c*+*a*⟩ slip {10$\bar{1}$1}⟨1$\bar{2}$10⟩	12	⟨13$\bar{8}\bar{5}$3⟩	12
Pyramidal II ⟨*c*+*a*⟩ slip {11$\bar{2}$2}⟨11$\bar{2}\bar{3}$⟩	6	⟨1$\bar{1}$00⟩	3

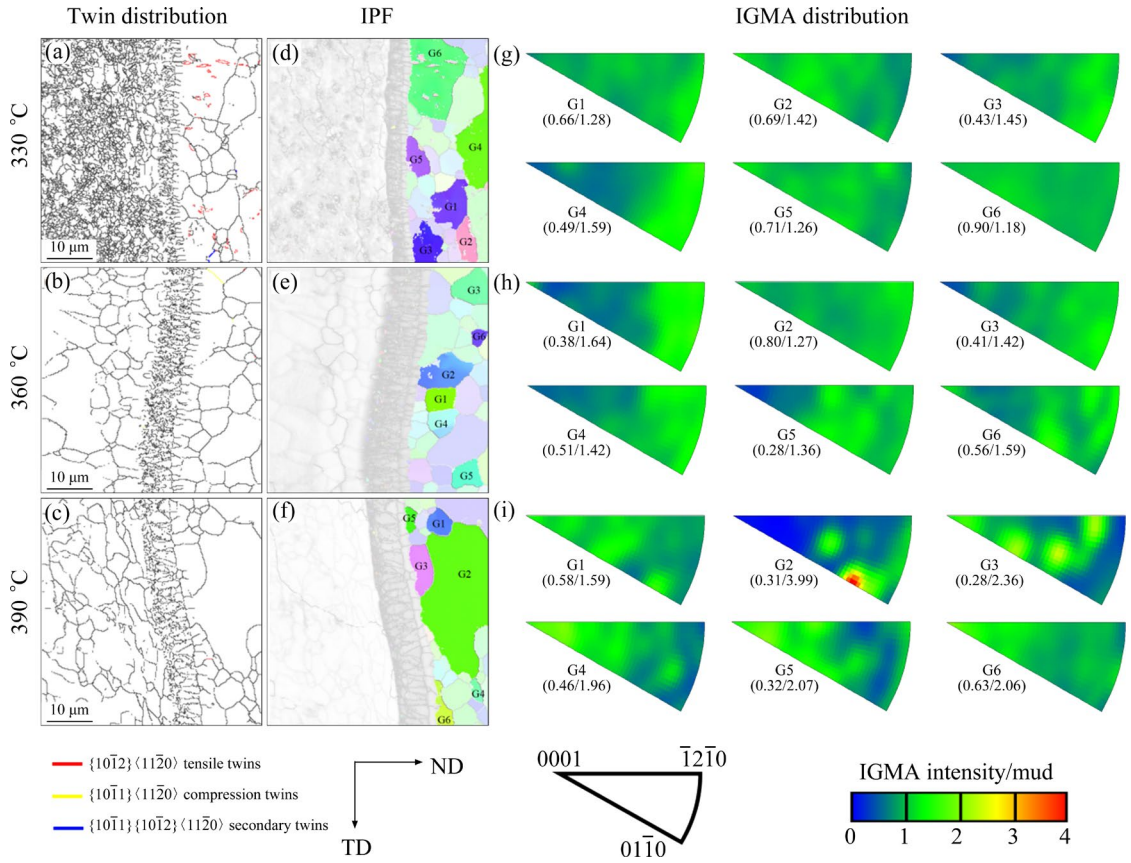

Fig. 13 Twin distribution (a−c), selected grains (d−f), and IGMA distribution of selected grains (g−i) at different temperatures

alloys is mainly coordinated by twinning and slip. However, at 360 °C, the twins are nearly absent, and the deformation mechanism of the magnesium alloy is mainly driven by various types of slip.

When the temperature reaches 390 °C, basal ⟨*a*⟩ or pyramidal II ⟨*c*+*a*⟩ slips, and prismatic ⟨*a*⟩ slip become the dominant slip systems in various slip systems, as illustrated in Fig. 13(i), it is possible to observe that Grain G5 exhibits ⟨0001⟩-type IGMA distribution, revealing that prismatic ⟨*a*⟩ slip dominates the deformation of this grain. Furthermore, Grains G2, G3, and G6 exhibit ⟨*uvt*0⟩-type IGMA distribution, and hence their deformation mechanisms are primarily dominated by basal ⟨*a*⟩ or pyramidal II ⟨*c*+*a*⟩ slips. Since basal ⟨*a*⟩ and pyramidal II ⟨*c*+*a*⟩ slips have the same Taylor axis, we further measured the SF value of all selected grains with basal ⟨*a*⟩ and pyramidal II ⟨*c*+*a*⟩ slips, as given in Table 5. The relative magnitudes of the SF values for basal ⟨*a*⟩ and pyramidal II ⟨*c*+*a*⟩ slips are compared to distinguish between slip systems with the same Taylor axis. It can be observed that at 390 °C, pyramidal II ⟨*c*+*a*⟩ slip dominates the deformation of Grain G6, while basal ⟨*a*⟩ slip dominates the deformation of Grains G2 and G3.

3.7 Effect of temperature on mechanical properties of Mg−Al composite rods

As depicted in Fig. 14(a), the microhardness of magnesium alloys and the bonding layer is significantly affected by temperature variations. Uniform, small-grained crystals can enhance the hardness of magnesium alloys, as previously analyzed in the DRX of magnesium alloys. Although the proportion of DRXed grains in the magnesium alloys is the highest at 390 °C, the mechanical properties of magnesium alloys decrease due to the continuous growth of a few DRXed grains at high temperatures. As temperature rises from 330 to 390 °C, the average hardness of magnesium alloys increases from HV 66.95 to HV 85.61 and then decreases to HV 75.00. The trend in hardness variation of the bonding layer is similar to that of the magnesium alloy, with the average hardness from HV 114.07 to HV 214.40,

Table 5 SF values of selected grains at different temperatures

Temperature/°C	Grain No.	SF value	
		Basal ⟨*a*⟩ slip {0001}⟨11$\bar{2}$0⟩	Pyramidal II ⟨*c*+*a*⟩ slip {11$\bar{2}$2}⟨11$\bar{2}$3⟩
330	G1	0.44	0.28
	G2	0.39	0.33
	G3	0.32	0.39
	G4	0.27	0.34
	G5	0.31	0.42
	G6	0.37	0.40
360	G1	0.38	0.36
	G2	0.49	0.15
	G3	0.28	0.45
	G4	0.31	0.44
	G5	0.43	0.42
	G6	0.44	0.33
390	G1	0.44	0.29
	G2	0.46	0.17
	G3	0.45	0.21
	G4	0.43	0.36
	G5	0.23	0.48
	G6	0.22	0.35

and then decreases to HV 155.72. Additionally, the hardness of aluminum alloys is also affected to some extent, but the average hardness remains stable in the range of HV 45−53.

As shown in Fig. 14(b), the bonding strength of the Mg−Al composite rods decreases from 15.54 to 8.32 MPa before rising to 12.71 MPa as the temperature increases. Furthermore, fracture analysis indicates that the fractures at 330 and 390 °C are relatively flat, exhibiting obvious cleavage steps, which are standard cleavage fractures. This further confirms that the IMCs between Mg and Al is a hard and brittle phase. However, at 360 °C, an apparent non-cleavage fracture morphology is observed. Tiny blocky grains are present, which are the primary features of intergranular fracture. EDS elemental analysis reveals that intergranular fractures occur mostly on the Al side at this temperature, as shown by the white dashed box in Figs. 15(c−d). The large shear stress in the ND at 360 °C causes the Mg−Al bonding layer to thicken while also increasing the hardness of the bonding layer significantly higher than that at the other two temperatures, resulting in an intergranular fracture of Mg−Al different from that observed at 330 and 390°C. In the preparation of Mg−Al composite materials, it is necessary to increase the bonding strength between Mg and Al while ensuring an increased proportion of DRX of Mg−Al.

Different temperatures induce varying degrees of changes in the yield strength and elongation of Mg−Al composite rods. Specifically, when the temperature is raised from 330 to 360°C, the elongation of the magnesium alloy increases from 13.3% to 14.4%, and the yield strength increases from 153 to 202 MPa, as illustrated in Fig. 14(c). However, when the temperature rises to 390 °C, the elongation drops to 13.1%, and the yield strength also decreases to 175 MPa. This observation is consistent with the previous analysis of the effect of temperature on the grains of the magnesium alloy. Furthermore, the presence of aluminum core provides larger shear stress to the magnesium alloy, which significantly increases the yield strength and elongation of magnesium alloy by 49 MPa and 2.1%, respectively. As depicted in Figs. 16(a, e), the

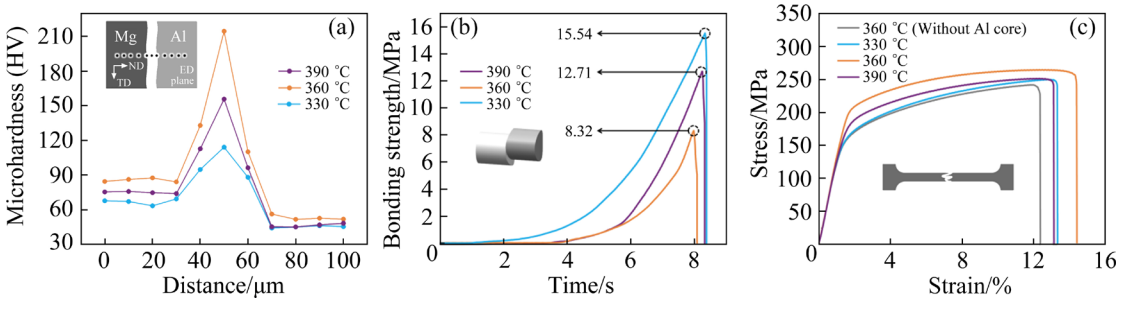

Fig. 14 Microhardness (a), bonding strength (b), and tensile mechanical properties (c) of magnesium alloys at different temperatures

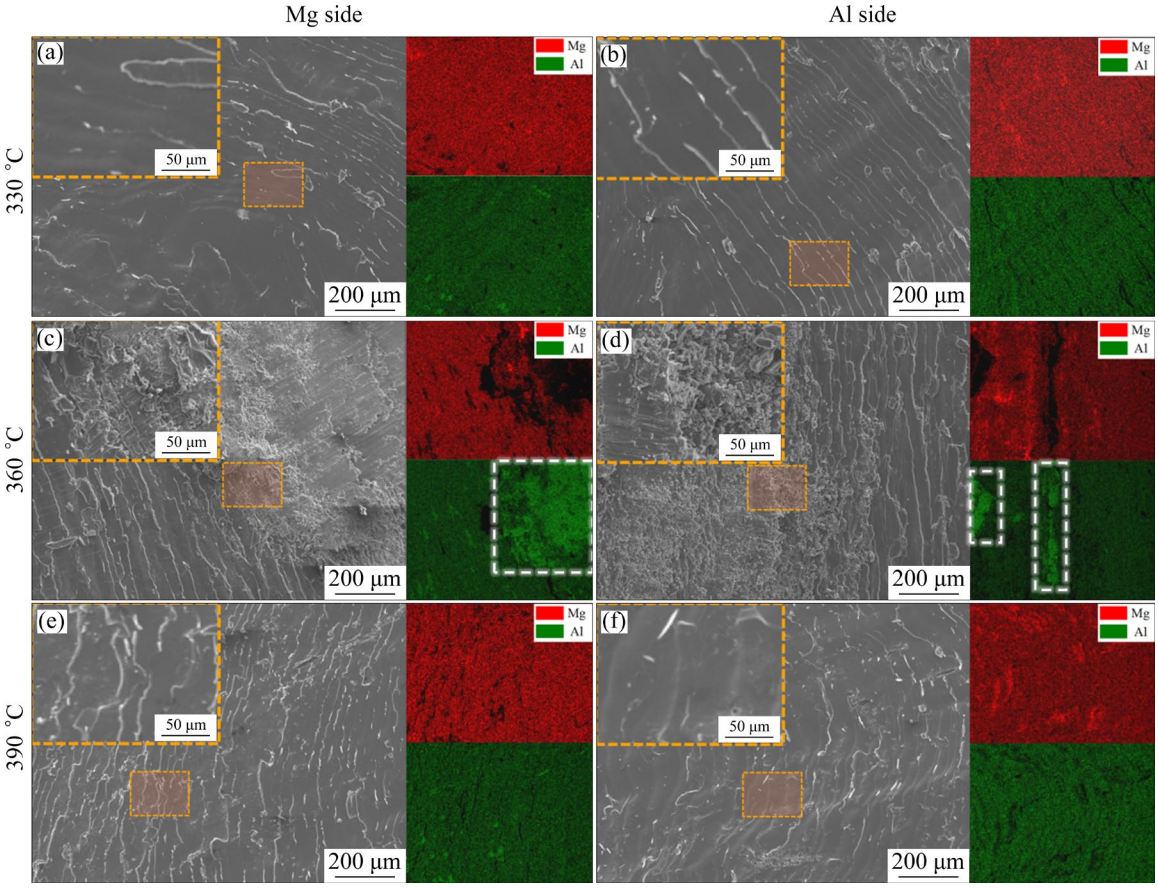

Fig. 15 Fracture morphologies of Mg side and Al side at different temperatures

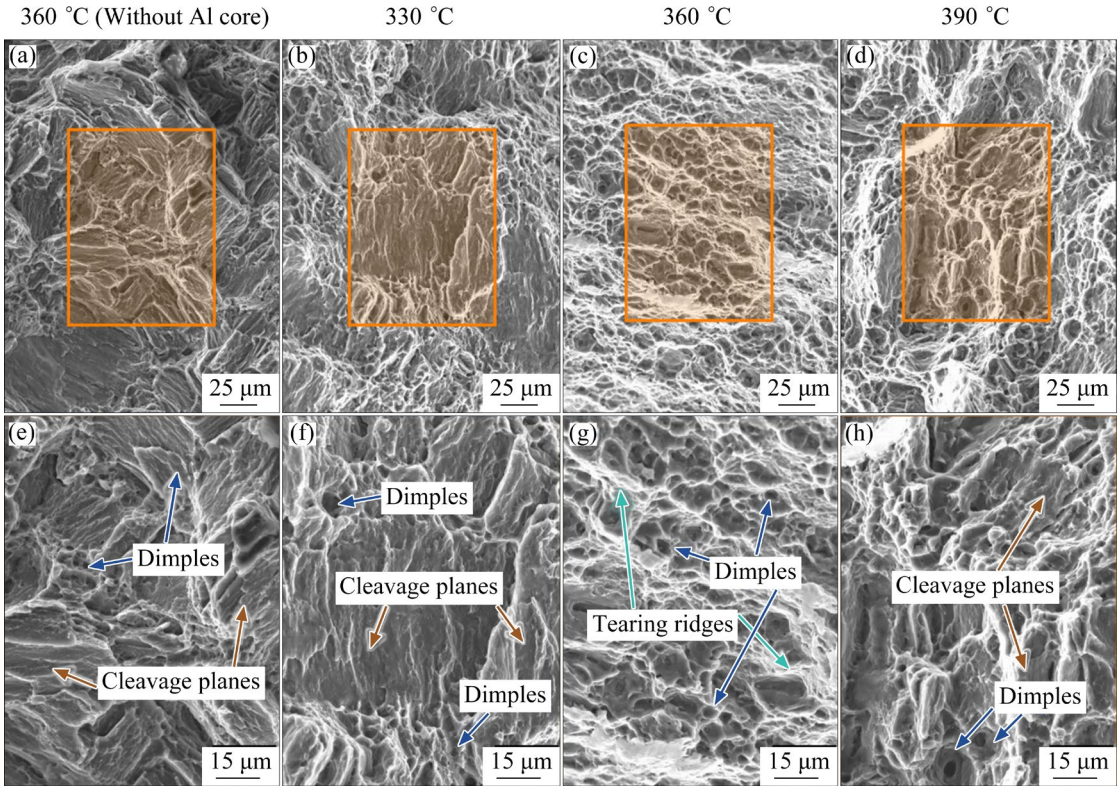

Fig. 16 Fracture morphologies of magnesium alloy at different temperatures and without Al core

fracture surfaces of magnesium alloys without Al core are mainly characterized by riverine and rocky morphologies, exhibiting evident cleavage planes. At 330 and 390°C, the dimples on the fracture surfaces of magnesium alloys significantly increase, presenting a mixed fracture pattern of both ductile and brittle characteristics, as shown in Figs. 16(b, f, d, h). This type of fracture is a hybrid fracture mode that possesses both toughness and brittleness. At 360 °C, the fracture surfaces of magnesium alloys are dominated by the distribution of dimples, and the depth and uniformity of the dimples significantly increase, as illustrated in Figs. 16(c, g). The diverse fracture morphologies also provide further evidence for the analysis of the tensile strength discussed earlier.

4 Conclusions

(1) The IMC on the Mg side of the bonding layer in Mg−Al composite rod is γ-$Al_{12}Mg_{17}$, while that on the Al side is β-Al_3Mg_2. Under the combined effects of shear stress and temperature, the diffusion of Al atoms on the Mg side increases at 360 °C, resulting in the maximum bonding layer thickness of 24 μm.

(2) Under shear stress, the textures of both Mg and Al alloys are attenuated. The grain orientation of the Al alloy becomes random. There exists a significant recrystallization texture in Al alloys at 360 °C. Brass {011}⟨211⟩, S {123}⟨634⟩, and R {124}⟨211⟩ textures appear at all three temperatures, with relatively uniform distribution.

(3) The DRX proportion of Al alloy increases and then decreases with increasing temperature as a consequence of the intricate effect of temperature and temperature-induced shear stresses. However, the DRX proportion of Mg alloy has consistently upward trend, and the DRX behavior of Mg alloy shifts from being dominated by DDRX, CDRX, and TDRX to being dominated by CDRX. The dislocations in the Mg alloy grains significantly decrease, and the average value of SF for basal ⟨*a*⟩ slip system in the Mg alloy increases from 0.34 to 0.41.

(4) With increasing temperature, the deformation mechanism of magnesium alloys varies from a coordinated initiation by twinning and slip, to various types of slip without a dominant slip system, and finally to the emergence of basal ⟨*a*⟩ or pyramidal II ⟨*c*+*a*⟩ slips, and prismatic ⟨*a*⟩ slip as the dominant slip system among the various slip systems.

(5) The bonding strength of the bonding layer is inversely proportional to its thickness and hardness. A unique phenomenon of fracture on the Al side occurs at 360 °C, and the yield strength and elongation of the magnesium alloy reach their maximum values of 202 MPa and 14.4%, respectively.

CRediT authorship contribution statement

Jian-xing ZHAO: Writing − Original draft, Investigation, Methodology, Data curation, Visualization; **Chao-wei ZENG:** Methodology, Software, Investigation, Validation; **Ting YUAN:** Methodology, Resources, Data curation; **Wei PENG:** Investigation, Validation; **Zhen-wei SUN:** Methodology, Visualization; **Ou ZHANG:** Methodology, Supervision, Formal analysis; **Hong-jun HU:** Funding acquisition, Project administration, Writing − Review & editing.

Declaration of competing interest

The authors declare that they have no known competing financial interests or personal relationships that could have appeared to influence the work reported in this paper.

Acknowledgments

This work was supported by the general project of the National Natural Science Foundation of China (No. 52071042), Chongqing Natural Science Foundation Project, China (Nos. CSTB2023NSCQ-MSX0079, cstc2021ycjh-bgzxm0148), and Graduate Student Innovation Program of Chongqing University of Technology, China (No. gzlcx20232008).

References

[1] YANG Yan, XIONG Xiao-ming, CHEN Jing, PENG Xiao-dong, CHEN Dao-lun, PAN Fu-sheng. Research advances in magnesium and magnesium alloys worldwide in 2020 [J]. Journal of Magnesium and Alloys, 2021, 9(3): 705−747.

[2] JEONG H T, KIM W J. Critical review of superplastic magnesium alloys with emphasis on tensile elongation behavior and deformation mechanisms [J]. Journal of Magnesium and Alloys, 2022, 10(5): 1133−1153.

[3] PRASAD S V S, PRASAD S B, VERMA K, MISHRA R K, KUMAR V, SINGH S. The role and significance of Magnesium in modern day research—A review [J]. Journal of Magnesium and Alloys, 2022, 10(1): 1−61.

[4] LIU Xiao, YANG Hui, ZHU Bi-wu, WU Yuan-zhi, LIU Wen-hui, TANG Chang-ping. Unveiling the mechanical response and accommodation mechanism of pre-rolled AZ31 magnesium alloy under high-speed impact loading [J]. Journal of Magnesium and Alloys, 2022, 10(4): 1096−1108.

[5] ZHU Bi-wu, LIU Xiao, XIE Chao, SU Jing, GUO Peng-cheng, TANG Chang-ping, LIU Wen-hui. Unveiling the underlying mechanism of forming edge cracks upon high strain-rate rolling of magnesium alloy [J]. Journal of Materials Science & Technology, 2020, 50: 59−65.

[6] ZHANG Cheng-hang, LI Zhuo, ZHANG Ji-kui, TANG Hai-bo, WANG Hua-ming. Additive manufacturing of magnesium matrix composites: Comprehensive review of recent progress and research perspectives [J]. Journal of Magnesium and Alloys, 2023, 11(2): 425−461.

[7] MENG Yun-peng, ZHANG Hua, LIN Bo-yu, WANG Li-fei, FAN Jian-feng, LU Li-wei, ZHOU Xin, HUANG Hai-liang, ZHANG Shan-zhou, ROVEN H J. Microstructure and mechanical properties of the AZ31/GW103K bimetal composite rods fabricated by co-extrusion [J]. Materials Science and Engineering A, 2022, 833: 142578.

[8] FENG Bo, XIN Yun-chang, YU Hui-hui, HONG Rui, LIU Qing. Mechanical behavior of a Mg/Al composite rod containing a soft Mg sleeve and an ultra hard Al core [J]. Materials Science and Engineering A, 2016, 675: 204−211.

[9] FENG Bo, XIN Yun-chang, SUN Zheng, YU Hui-hui, WANG Juan, LIU Qing. On the rule of mixtures for bimetal composites [J]. Materials Science and Engineering A, 2017, 704: 173−180.

[10] FENG Bo, XIN Yun-chang, HONG Rui, YU Hui-hui, WU Yang, LIU Qing. The effect of architecture on the mechanical properties of Mg−3Al−1Zn rods containing hard Al alloy cores [J]. Scripta Materialia, 2015, 98: 56−59.

[11] FENG Bo, XIN Yun-chang, GUO Fei-long, YU Hui-hui, WU Yang, LIU Qing. Compressive mechanical behavior of Al/Mg composite rods with different types of Al sleeve [J]. Acta Materialia, 2016, 120: 379−390.

[12] FENG Bo, FENG Xiao-wei, YAN Chang-jian, XIN Yun-chang, WANG Hai-yan, WANG Juan, ZHENG Kai-hong. On the rule of mixtures for bimetal composites without bonding [J]. Journal of Magnesium and Alloys, 2020, 8(4): 1253−1261.

[13] SEN M, PURI A B. Formation of intermetallic compounds (IMCs) in FSW of aluminum and magnesium alloys (Al/Mg alloys)—A review [J]. Materials Today Communications, 2022, 33: 105017.

[14] LIU Ting-ting, SONG Bo, HUANG Guang-sheng, JIANG Xian-quan, GUO Sheng-feng, ZHENG Kai-hong, PAN Fu-sheng. Preparation, structure and properties of Mg/Al laminated metal composites fabricated by roll-bonding: A review [J]. Journal of Magnesium and Alloys, 2022, 10(8): 2062−2093.

[15] TANG Jian-wei, CHEN Liang, ZHAO Guo-qun, ZHANG Cun-sheng, SUN Lu. Achieving three-layered Al/Mg/Al sheet via combining porthole die co-extrusion and hot forging [J]. Journal of Magnesium and Alloys, 2020, 8(3): 654−666.

[16] GUO Li-li, WANG Jian-qiang, YUN Xin-bing, CHEN Zhong-chun. Fabrication of aluminum–magnesium clad composites by continuous extrusion [J]. Materials Science and Engineering A, 2021, 802: 140670.

[17] SKORPEN K G, MAULAND E, REISO O, ROVEN H J. Novel method of screw extrusion for fabricating Al/Mg (macro-) composites from aluminum alloy 6063 and magnesium granules [J]. Transactions of Nonferrous Metals Society of China, 2014, 24(12): 3886−3893.

[18] FENG Bo, SUN Zheng, WU Yang, FENG Xiao-wei, WANG Juan, ZHENG Kai-hong. Microstructure and mechanical behavior of Mg ZK60/Al 1100 composite plates fabricated by co-extrusion [J]. Journal of Alloys and Compounds, 2020, 842: 155676.

[19] BAI Sheng-wen, LIU Lin-tao, LI Kun, JIANG Bin, HUANG Guang-sheng, ZHANG Ding-fei, PAN Fu-sheng. Investigation into the microstructure, tensile properties and bendability of Mg–Al–Zn/Mg–*x*Gd laminated composite sheets extruded by porthole die [J]. Journal of Materials Research and Technology, 2022, 21: 12−29.

[20] YANG Bo-wei, WANG Yu, GAO Min-qiang, WANG Chang-feng, GUAN Ren-guo. Microstructural evolution and strengthening mechanism of Al−Mg alloys with fine grains processed by accumulative continuous extrusion forming [J]. Journal of Materials Science & Technology, 2022, 128: 195−204.

[21] CROTEAU J R, JUNG J G, WHALEN S A, DARSELL J, MELLO A, HOLSTINE D, LAY K, HANSEN M, DUNAND D C, VO Nhon Q. Ultrafine-grained Al−Mg−Zr alloy processed by shear-assisted extrusion with high thermal stability [J]. Scripta Materialia, 2020, 186: 326−330.

[22] CHEN Cai, HAN Dong-sheng, WANG Ming-chuan, XU Shun, CAI Ting, YANG Sen, SHI Feng-jian, BEAUSIR B, TOTH L S. High strength and high ductility of Mg−10Gd−3Y alloy achieved by a novel extrusion-shearing process [J]. Journal of Alloys and Compounds, 2023, 931: 167498.

[23] TIAN Ye, HU Hong-jun, ZHAO Hui, ZHANG Wei, LIANG Peng-cheng, JIANG Bin, ZHANG Ding-fei. An extrusion−shear−expanding process for manufacturing AZ31 magnesium alloy tube [J]. Transactions of Nonferrous Metals Society of China, 2022, 32(8): 2569−2577.

[24] WANG Bo-ning, WANG Feng, WANG Zhi, LIU Zheng, MAO Ping-li. Fabrication of fine-grained, high strength and toughness Mg alloy by extrusion−shearing process [J]. Transactions of Nonferrous Metals Society of China, 2021, 31(3): 666−678.

[25] TIAN Ye, HU Hong-jun, LI Yang, ZHAO Jian-xing, HONG Xing, JIANG Bin, ZHANG Ding-fei. A continuous extrusion−shear (ES) composite process for significantly improving the metallurgical bonding and textures regulations and grain refinements of Al/Mg bimetallic composite rods [J]. Advanced Engineering Materials, 2022, 24(6): 2200061.

[26] ZHANG Wei, HU Hong-jun, HU Gang, SUN Zhen-wei, YUAN Ting, OU Zhong-wen. A direct extrusion-shear

deformation composite process that significantly improved the metallurgical bonding and texture regulation grain refinement and mechanical properties of hot-extruded AZ31/AA6063 composite tubes [J]. Materials Science and Engineering A, 2023, 880: 145090.

[27] LIU Wen-hong, BAO Jia-xin, QIAO Ming-liang, YIN Si-qi, WANG Zhan-kun, CUI Jian-zhong, ZHANG Zhi-qiang. Microstructures and mechanical properties of Mg−6Zn−1Y−0.85Zr alloy prepared at different extrusion temperatures and speeds [J]. Journal of Materials Research and Technology, 2022, 21: 1042−1052.

[28] LIU Shuai-shuai, LIU Han, ZHANG Bao-xuan, HUANG Guang-sheng, CHEN Xiang, TANG Ai-tao, JIANG Bin, PAN Fu-sheng. Effects of extrusion temperature on microstructure evolution and mechanical properties of heterogeneous Mg−Gd alloy laminates via accumulated extrusion bonding [J]. Transactions of Nonferrous Metals Society of China, 2022, 32(7): 2190−2204.

[29] YU Zi-jian, XU Chao, MENG Jian, LIU Ke, FU Jin-long, KAMADO S. Effects of extrusion ratio and temperature on the mechanical properties and microstructure of as-extruded Mg−Gd−Y−(Nd/Zn)−Zr alloys [J]. Materials Science and Engineering A, 2019, 762: 138080.

[30] KIM S H, LEE S W, MOON B G, KIM H S, KIM Y M, PARK S H. Influence of extrusion temperature on dynamic deformation behaviors and mechanical properties of Mg−8Al−0.5Zn−0.2Mn−0.3Ca−0.2Y alloy [J]. Journal of Materials Research and Technology, 2019, 8(6): 5254−5270.

[31] XU Yu-zhao, LI Jing-yuan, QI Ming-fan, GUO Wen-hui, DENG Yue. A newly developed Mg−Zn−Gd−Mn−Sr alloy for degradable implant applications: Influence of extrusion temperature on microstructure, mechanical properties and in vitro corrosion behavior [J]. Materials Characterization, 2022, 188: 111867.

[32] WU Xiao-feng, XU Chun-xiang, ZHANG Zheng-wei, YANG Wen-fu, ZHANG Jing-shan. Microstructure evolution, strengthening mechanisms and deformation behavior of high-ductility Mg−3Zn−1Y−1Mn alloy at different extrusion temperatures [J]. Transactions of Nonferrous Metals Society of China, 2023, 33(2): 422−437.

[33] MALIK A, WANG Yang-wei, HUANWU Cheng, NAZEER F, AHMED B, KHAN M A, MINGJUN Wang. Constitutive analysis, twinning, recrystallization, and crack in fine-grained ZK61 Mg alloy during high strain rate compression over a wide range of temperatures [J]. Materials Science and Engineering A, 2020, 771: 138649.

[34] SHENG Kun, LU Li-wei, XIANG Yao, MA Min, WU Zhi-qiang. Crack behavior in Mg/Al alloy thin sheet during hot compound extrusion [J]. Journal of Magnesium and Alloys, 2019, 7(4): 717−724.

[35] BAE J H, PRASADA RAO A K, KIM K H, KIM N J. Cladding of Mg alloy with Al by twin-roll casting [J]. Scripta Materialia, 2011, 64(9): 836−839.

[36] ACARER M, DEMIR B, DIKICI B, SALUR E. Microstructure, mechanical properties, and corrosion resistance of an explosively welded Mg−Al composite [J]. Journal of Magnesium and Alloys, 2022, 10(4): 1086−1095.

[37] KUMAR S, WU Chuan-song. Eliminating intermetallic compounds via Ni interlayer during friction stir welding of dissimilar Mg/Al alloys [J]. Journal of Materials Research and Technology, 2021, 15: 4353−4369.

[38] ZHU Bo, LIANG Wei, LI Xian-rong. Interfacial microstructure, bonding strength and fracture of magnesium–aluminum laminated composite plates fabricated by direct hot pressing [J]. Materials Science and Engineering A, 2011, 528(21): 6584−6588.

[39] ZHANG X P, CASTAGNE S, YANG T H, GU C F, WANG J T. Entrance analysis of 7075 Al/Mg−Gd−Y−Zr/7075 Al laminated composite prepared by hot rolling and its mechanical properties [J]. Materials & Design, 2011, 32: 1152−1158.

[40] JAFARIAN M, KHODABANDEH A, MANAFI S. Evaluation of diffusion welding of 6061 aluminum and AZ31 magnesium alloys without using an interlayer [J]. Materials & Design (1980—2015), 2015, 65: 160−164.

[41] FUNAMIZU Y, WATANABE K. Interdiffusion in the Al–Mg system [J]. Transactions of the Japan Institute of Metals, 1972, 13(4): 278−283.

[42] SEQUEIRA C A C, AMARAL L. Role of Kirkendall effect in diffusion processes in solids [J]. Transactions of Nonferrous Metals Society of China, 2014, 24(1): 1−11.

[43] HOOSHMAND M S, ZHONG W, ZHAO J C, WINDL W, GHAZISAEIDI M. Data on the comprehensive first-principles diffusion study of the aluminum−magnesium system [J]. Data in Brief, 2020, 30: 105381.

[44] BRENNAN S, BERMUDEZ K, KULKARNI N S, SOHN Y. Interdiffusion in the Mg−Al system and intrinsic diffusion in β-Mg_2Al_3 [J]. Metallurgical and Materials Transactions A, 2012, 43(11): 4043−4052.

[45] ZHONG Wei, HOOSHMAND M S, GHAZISAEIDI M, WINDL W, ZHAO Ji-cheng. An integrated experimental and computational study of diffusion and atomic mobility of the aluminum–magnesium system [J]. Acta Materialia, 2020, 189: 214−231.

[46] SAUVAGE X, WETSCHER F, PAREIGE P. Mechanical alloying of Cu and Fe induced by severe plastic deformation of a Cu−Fe composite [J]. Acta Materialia, 2005, 53(7): 2127−2135.

[47] LI Jian-yu, LÜ Shu-lin, ZHAO Di-jia, CHEN Lu, PAN Yu, GUO Wei, WU Shu-sen. Preparation of Mg_2Si/Al−Cu composite under a novel continuous squeeze casting-extrusion process assisted with ultrasonic treatment [J]. Materials Science and Engineering A, 2023, 862: 144469.

[48] SHEN Jing-yuan, ZHANG Ling-yu, HU Lian-xi, SUN Yu, GAO Fei, LIU Wen-chao, YU Huan. Effect of subgrain and the associated DRX behaviour on the texture modification of Mg−6.63Zn−0.56Zr alloy during hot tensile deformation [J]. Materials Science and Engineering A, 2021, 823: 141745.

[49] NIE Hui-hui, HAO Xin-wei, CHEN Hong-sheng, KANG Xiao-ping, WANG Taolue, MI Yu-jie, LIANG Wei. Effect of twins and dynamic recrystallization on the microstructures and mechanical properties of Ti/Al/Mg laminates [J].

Materials & Design, 2019, 181: 107948.
[50] CHUN Y B, DAVIES C H J. Investigation of prism ⟨*a*⟩ slip in warm-rolled AZ31 alloy [J]. Metallurgical and Materials Transactions A, 2011, 42(13): 4113−4125.
[51] LV Hao, LI Lu, WEN Zhuo-zhang, LIU Chun-rong, ZHOU Wei, BAI Xue, ZHONG Hui-ling. Effects of extrusion ratio and temperature on the microstructure and mechanical properties of Mg−Zn−Yb−Zr extrusion alloys [J]. Materials Science and Engineering A, 2022, 833: 142521.
[52] CHUN Y B, BATTAINI M, DAVIES C H J, HWANG S K. Distribution characteristics of in-grain misorientation axes in cold-rolled commercially pure titanium and their correlation with active slip modes [J]. Metallurgical and Materials Transactions A, 2010, 41(13): 3473−3487.

Mg−Al 复合棒材中剪切应力和挤压温度之间的相互作用

赵健行，曾朝伟，袁 婷，彭 威，孙振威，章 欧，胡红军

重庆理工大学 材料科学与工程学院，重庆 400054

摘 要：采用挤压−剪切(ES)工艺制备铝芯增强镁合金的 Mg−Al 复合棒材，并研究在不同挤压温度和剪切应力下 Mg−Al 复合棒材的显微组织、变形机制和力学性能。实验结果表明，Al 和 Mg 合金的动态再结晶(DRX)比例和织构由温度和剪切应力共同控制。铝合金的织构类型在不同温度下表现出轻微的变化。随着温度的升高，镁合金的 DRX 行为从不连续 DRX(DDRX)、连续 DRX(CDRX)和孪晶诱导 DRX(TDRX)向 CDRX 转变，镁合金晶粒中的位错密度显著降低，基面⟨*a*⟩滑移系的施密特因子(SF)平均值增加，特别是部分晶粒在 390 ℃时表现出明显的主导滑移系。由于温度和剪切应力的相互影响，镁合金的结合层硬度和厚度以及屈服强度和伸长率在 360 ℃时达到最大值。

关键词：Mg−Al 复合棒材；织构演变；变形机制；金属间化合物；挤压−剪切工艺

(Edited by Bing YANG)